

# Infrared Observational Manifestations of Young Dusty Super Star Clusters

Sergio Martínez-González<sup>1</sup>, Guillermo Tenorio-Tagle<sup>1</sup>, Sergiy Silich<sup>1</sup>

## ABSTRACT

The growing evidence pointing at core-collapse supernovae as large dust producers makes young massive stellar clusters ideal laboratories to study the evolution of dust immersed into a hot plasma. Here we address the stochastic injection of dust by supernovae and follow its evolution due to thermal sputtering within the hot and dense plasma generated by young stellar clusters. Under these considerations, dust grains are heated by means of random collisions with gas particles which results on the appearance of infrared spectral signatures. We present time-dependent infrared spectral energy distributions which are to be expected from young stellar clusters. Our results are based on hydrodynamic calculations that account for the stochastic injection of dust by supernovae. These also consider gas and dust radiative cooling, stochastic dust temperature fluctuations, the exit of dust grains out of the cluster volume due to the cluster wind and a time-dependent grain size distribution.

*Subject headings:* galaxies: star clusters: general — (ISM:) dust, extinction — Physical Data and Processes: hydrodynamics

## 1. Introduction

The idea of core-collapse supernovae as major dust producers was first envisaged in the pioneering work of Cernuschi, Marsicano, & Codina (1967). They showed that the effective condensation of refractory elements due to the large variation of temperature in the ejecta of core-collapse supernovae can lead to the formation of massive quantities of dust. However, it took more than two decades until SN1987A provided the first direct evidence for the condensation of iron into dust grains (Moseley et al. 1989; Suntzeff & Bouchet 1990; Wooden et al. 1993; Bautista et al. 1995, and references therein) in the SN ejecta. According to Todini & Ferrara (2001) and Nozawa et al. (2003), one can expect the formation of

---

<sup>1</sup>Instituto Nacional de Astrofísica Óptica y Electrónica, AP 51, 72000 Puebla, México; sergiomtz@inaoep.mx

( $0.1 - 1$ )  $M_{\odot}$  of dust in the first decades after a type II SN event while a dust mass fraction between 0.2-1.0 would be destroyed by the supernova reverse shock before being injected into the ISM (Nozawa et al. 2007). Also, the dust composition consists mostly of silicates and carbon (see conflicting interpretations of which composition is dominant by Matsuura et al. (2015) and Dwek & Arendt (2015)).

These predictions find strong support in recent Herschel and ALMA observations of nearby supernova remnants like the Crab Nebula, Cassiopeia A and SN1987A. Gomez et al. (2012) found evidence for the presence of  $0.1 - 0.25 M_{\odot}$  of ejected dust in the Crab Nebula, a value that is orders of magnitude larger than what was obtained with Spitzer data (Temim et al. 2012). Barlow et al. (2010) estimated  $0.075 M_{\odot}$  of cool dust ( $\sim 35$  K) in the ejecta of Cassiopeia A, however, due to high cirrus contamination along the line of sight, they were not able to identify the presence of cold dust ( $\sim 20$  K) which can increase the content of dust in the ejecta to values in the range of  $0.5 - 1.0 M_{\odot}$  (Gomez 2013). More recently, Arendt et al. (2014) estimated the total mass of dust in the shocked ISM and ejecta regions of Cassiopeia A to be  $0.04 M_{\odot}$ , and  $\lesssim 0.1 M_{\odot}$  in the unshocked ejecta.

Indebetouw et al. (2014) and Matsuura et al. (2014) fitted the spectral energy distribution of SN1987A and derived  $\sim 0.8 M_{\odot}$  of newly formed dust in the ejecta of the supernova with  $\sim 0.3 M_{\odot}$  of amorphous carbon and  $\sim 0.5 M_{\odot}$  of silicates. On the other hand, Dwek & Arendt (2015) derived a total mass of dust after day 8500 after the explosion of SN1987A consisting of  $\sim 0.4 M_{\odot}$  of silicates and  $\sim 0.05 M_{\odot}$  of amorphous carbon.

The large SN rate expected in super star clusters (SSCs) (a few thousand SN events during the type II SN era for a  $10^5 M_{\odot}$  star cluster), together with the large production and injection of dust, implies a frequent replenishment of dust inside the star cluster volume (Tenorio-Tagle et al. 2013). In such clusters, the thermalization of the matter reinserted by massive stars and SNe inside young and massive star clusters leads to a large central overpressure and the launching of hot ( $\sim 10^7$  K) and dense ( $\sim (1 - 1000) \text{ cm}^{-3}$ ) star cluster winds (Chevalier & Clegg 1985; Tenorio-Tagle et al. 2007).

These considerations make super star clusters ideal places to heat newly injected dust grains due to the transfer of thermal energy from the gas via stochastic collisions with electrons and nuclei as discussed by Dwek (1986).

Dust grains then cool down in a short time scale and re-emit the obtained energy in the infrared regime. This is a very effective cooling mechanism for the hot and dusty gas which can surpass the cooling from a gas in collisional ionization equilibrium by several orders of magnitude (Ostriker & Silk 1973; Dwek & Werner 1981; Dwek 1987; Smith et al. 1996; Guillard et al. 2009). Infrared excesses have been observed in a considerable num-

ber of star clusters in low-metallicity blue compact dwarf galaxies, e.g: SBS 0335-052E, Haro 11, Mrk 930 and I Zw18 (Vanzi et al. 2000; Adamo et al. 2010a,b, 2011; Fisher et al. 2014; Izotov et al. 2014). From these studies, Vanzi et al. (2000); Reines et al. (2008) and Izotov et al. (2014), have invoked a hot dust component ( $\sim 800$  K) in order to explain the near-infrared spectral energy distributions observed in the bright SSCs 1 and 2 in SBS 0335-052.

Here we combine Dwek’s (1986; 1987) stochastic dust heating and cooling prescriptions with our steady-state wind hydrodynamic model to propose several scenarios of dust injection and its influence on the spectral energy distributions (SEDs) from starburst regions. To follow the evolution of the dust size distribution, and therefore the evolution of the SEDs, it is crucial to notice that the stellar winds are steady but the rate of supernova makes the dust injection an stochastic process. Dust is injected by stochastic supernova events into the intracluster medium, collisionally heated and eroded before the next injection episode. Moreover, we consider the exit of dust grains as they stream out, coupled to the gas, from the starburst region.

The paper is organized as follows: in Section 2 we describe our star cluster, star cluster wind and time-dependent dust size distribution models, and formulate our assumptions regarding the dust grain physics and composition. In Section 3, we use the hydrodynamic results together with the physics of stochastic dust heating and cooling to obtain the expected spectral energy distributions of young stellar clusters. In Section 4 we summarize our results and outline our conclusions. Complementary information about the dust cooling model and stochastic dust temperature fluctuations are presented in Appendix A.1 and Appendix A.2.

## 2. Star Cluster Winds and Dust Injection

We consider young and massive star clusters in which massive stars follow a generalized Schuster stellar density distribution,  $\rho_* \propto [1+(r/R_c)^2]^{-\beta}$ , (Palouš et al. 2013; Tenorio-Tagle et al. 2013, 2015) with  $\beta = 1.5$ , where  $r$  is the distance from the cluster center and  $R_c$  is the core radius of the stellar distribution. This stellar distribution is truncated at radius  $R_{SC}$ , the star cluster surface. Both,  $R_c$  and  $R_{SC}$ , define the degree of compactness of the star cluster, which can be measured by the radius at which half of the star cluster mass is located,  $R_{hm}$ . Similarly to Tenorio-Tagle et al. (2013), we consider star clusters in which other input parameters are: the star cluster mechanical luminosity,  $L_{SC}$ , and the adiabatic wind terminal speed  $V_{A\infty}$ , which are related to the mass deposition rate  $\dot{M} = 2L_{SC}/V_{A\infty}^2$ . We assume that the mechanical luminosity scales with the total mass of the star cluster,  $M_{SC}$ , as  $L_{SC} = 3 \times 10^{39}(M_{SC}/10^5 M_\odot)$  erg s $^{-1}$  (Leitherer et al. 1999).

In our approach, supernova explosions inject dust uniformly throughout the cluster with a standard Mathis et al. (1977, hereafter MRN) grain size distribution (dust grain number density in the size interval  $a$  and  $a + \Delta a$ ):

$$\frac{\partial n_i^{inj}}{\partial a} = A_i^{(m)} a^{-\alpha}, \quad a_{min} \leq a \leq a_{max}, \quad (1)$$

where  $a_{min}$  and  $a_{max}$  are the minimum grain size and cut-off value of the size distribution. In this definition, subindex  $i$  is used to distinguish between dust species, in our case graphite and silicate, and subindex  $m$  numbers the consecutive dust injection events.

Table 1: Dust Properties

Symbol	Silicate	Graphite	Definition
$\rho_{gr}$	3.3	2.26	Dust grain density ( $\text{g cm}^{-3}$ ) <sup>(1)</sup>
$\alpha$	3.5	3.5	Power index of the MRN distribution
$f_i$	0.5	0.5	Mass fraction of the grain species

<sup>(1)</sup> Hirashita & Nozawa (2013).

The normalization factors,  $A_i^{(m)}$  (with units  $\text{cm}^{\alpha-4}$ ), are obtained from the condition:

$$A_i^{(m)} = \frac{f_i M_{dSN}^{(m)} / V_{SC}}{\int_{a_{min}}^{a_{max}} \frac{4}{3} \pi \rho_{gr} a^{3-\alpha} da}, \quad (2)$$

where  $\rho_{gr}$  is the dust grain density,  $f_i$  is the mass fraction of the silicate and graphite species,  $M_{dSN}^{(m)}$  is the total mass of dust injected in a single supernova event and  $V_{SC}$  is the star cluster volume. Table 1 summarizes the input parameters for the injected dust size distribution and the characteristics of the dust species, in our case, graphite and silicate grains.

The dust lifetime against thermal sputtering at temperatures above  $10^6$  is defined as  $\tau_{sput} = a/|\dot{a}|$ ; where  $\dot{a}$ , the rate at which the dust grain with radius  $a$  decreases with time  $t$  when it is immersed into a hot plasma with temperature  $T$  and density  $n$ , is given by (Tsai & Mathews 1995):

$$\dot{a} = \frac{da}{dt} = -1.4nh \left[ \left( \frac{T_s}{T} \right)^w + 1 \right]^{-1}, \quad (3)$$

which leads to:

$$\tau_{sput} = 7.07 \times 10^5 \frac{a(\mu\text{m})}{n(\text{cm}^{-3})} \left[ \left( \frac{T_s}{T} \right)^w + 1 \right] \text{ yr}, \quad (4)$$

where  $h$ ,  $T_s$  and  $w$  are constants with values  $h = 3.2 \times 10^{-18} \text{ cm}^4 \text{ s}^{-1}$ ,  $T_s = 2 \times 10^6 \text{ K}$  and  $w = 2.5$ . These formulas are an approximation to the detailed calculations of Draine & Salpeter (1979) and Tielens et al. (1994) for graphite and silicate grains. The continuity equation which governs the evolution of the dust size distribution due to thermal sputtering is (Laor & Draine 1993; Yamada & Kitayama 2005):

$$\dot{a} \frac{\partial}{\partial a} \left( \frac{\partial n_i}{\partial a} \right) + \frac{\partial}{\partial t} \left( \frac{\partial n_i}{\partial a} \right) = \begin{cases} A_i^{(m)} a^{-\alpha} / \tau_{inj}^{(m)}, & \text{if } t \leq \tau_{SN}^{(m)} + \tau_{inj}^{(m)}, \\ 0, & \\ A_i^{(m)} a^{-\alpha} / \tau_{inj}^{(m)}, & \text{if } t > \tau_{SN}^{(m)} + \tau_{inj}^{(m)}, \end{cases} \quad (5)$$

where the first case applies for a constant MRN dust injection during a timescale  $\tau_{inj}^{(m)}$  after the  $m$ -supernova event has occurred (at  $t = \tau_{SN}^{(m)}$ ); and the second case considers that the  $m$ -supernova dust injection has ceased. The solutions of equations (5) after the  $n$ -supernova event (the last event considered) are then:

$$\frac{\partial n_i}{\partial a} = \begin{cases} \sum_{m=1}^n \frac{A_i^{(m)}}{\tau_{inj}^{(m)} \dot{a}} \left[ \frac{a^{-\alpha+1}}{(-\alpha+1)} - \frac{[a - \dot{a}(t - \tau_{SN}^{(m)})]^{-\alpha+1}}{(-\alpha+1)} \right], & \text{if } t \leq \tau_{SN}^{(m)} + \tau_{inj}^{(m)}, \\ \sum_{m=1}^n \frac{A_i^{(m)}}{\tau_{inj}^{(m)} \dot{a}} \left[ \frac{[a - \dot{a}(t - \tau_{SN}^{(m)} - \tau_{inj}^{(m)})]^{-\alpha+1}}{(-\alpha+1)} - \frac{[a - \dot{a}(t - \tau_{SN}^{(m)})]^{-\alpha+1}}{(-\alpha+1)} \right], & \text{if } t > \tau_{SN}^{(m)} + \tau_{inj}^{(m)}, \end{cases} \quad (6)$$

with the conditions that  $A_i^{(m)} = 0$  until the  $m$ -supernova event occurs and the mass of dust at  $t = \tau_{SN}^{(1)} = 0$  equals zero. These general solutions take into account the residual mass of dust from the previous injections and the evolved dust size distribution associated to them.

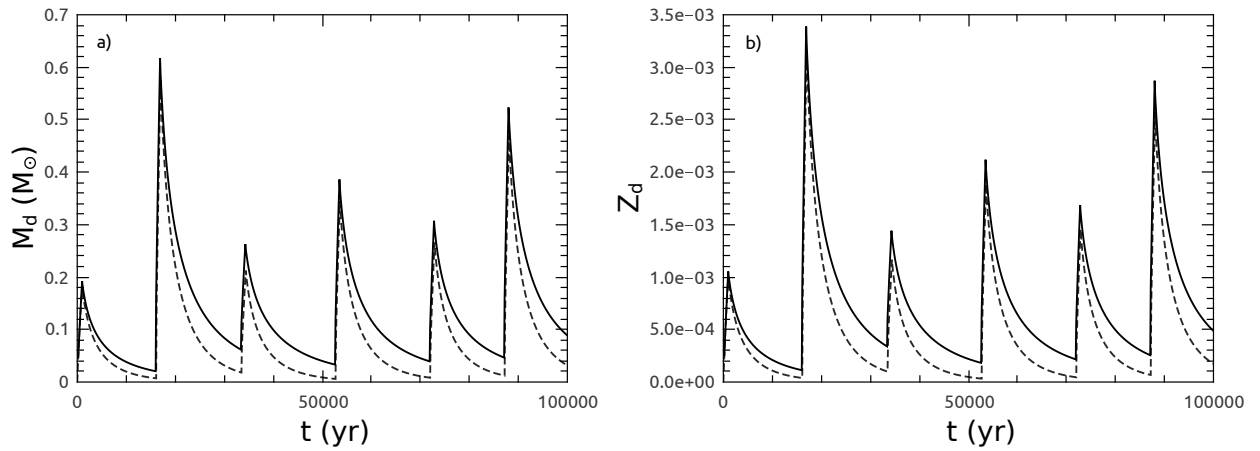


Fig. 1.— Evolution of the dust mass and dust-to-gas mass ratio with and without the exit of dust grains from the starburst region. Panels a) and b) show the residual  $M_d(t)$  and dust-to-gas mass ratio, respectively, from 6 injection events with account of thermal sputtering. Solid lines depict the case when dust grains are subject to thermal sputtering; dashed lines consider also the case when dust is expelled out of the star cluster. This case corresponds to a  $3 \times 10^5 M_\odot$  cluster with  $V_{\infty A} = 1000 \text{ km s}^{-1}$ ,  $R_{SC} = 5 \text{ pc}$  and  $R_c = 4 \text{ pc}$ . The values of  $M_{dSN}^{(m)}$  and the interval between consecutive supernova events  $\Delta T_{SN}^{(m)}$  were pseudo-randomly selected. Note that the exit of dust grains in the cluster wind leads to a more rapid depletion of dust.

Note that the asymptotic behavior in these solutions is similar to that derived by Dwek et al. (2008) for the case of grain destruction with a continuous injection.

The total mass of dust for each dust species as a function of time is then:

$$M_d(t) = \frac{4\pi}{3} \rho_{gr} V_{SC} \int_{a_{min}}^{a_{max}} a^3 \frac{\partial n_i}{\partial a} da, \quad (7)$$

which implies a time-dependent dust-to-gas mass ratio given by:

$$Z_d(t) = \frac{4\pi}{3} \frac{\rho_{gr}}{\rho} \int_{a_{min}}^{a_{max}} a^3 \frac{\partial n_i}{\partial a} da, \quad (8)$$

where  $\rho = 1.4m_H n$  is the gas mass density and  $m_H$  is the hydrogen mass.

The above equations do not take into account that dust, independent of its size, is expelled out from the cluster and thus  $A_i^{(m)}$  is no longer a constant. The rate at which dust is ejected from the cluster is  $\dot{M}_d(t) = 4\pi R_{SC}^2 \rho c_s Z_d(t)$ ; where  $c_s$  is the outflow's local sound speed obtained from the wind hydrodynamical calculations.

In order to consider dust outflowing from the cluster, we have taken a finite differences approach described as follows: (1) calculate  $M_d(t)$  with the original value of  $A_i^{(m)}$  at  $t = \tau_{SN}^{(m)} + \Delta t$ ; (2) at the next time-step,  $t = \tau_{SN}^{(m)} + 2\Delta t$ , subtract  $\dot{M}_d(t)\Delta t$  to  $M_d(t)$  and with this mass, replace  $A_i^{(m)}$  with

$$A_i^{(m)'} = \frac{f_i \left[ M_d(t) - \dot{M}_d(t)\Delta t \right] / V_{SC}}{\frac{1}{A_i^{(m)}} \int_{a_{min}}^{a_{max}} \frac{4}{3} \pi \rho_{gr} a^3 \frac{\partial n_i}{\partial a}(t) da}; \quad (9)$$

(3) repeat the procedure for every time-step and for the normalization constants associated to each supernova dust injection. In our calculations, we have taken  $\Delta t = 100$  yr and  $\tau_{inj}^{(m)} = \tau_{inj} = 1000$  yr (the same timescale for every dust injection). We tested this method compared to the analytic solution (equations 1-8), in the case when  $\dot{M}_d(t) = 0$ , and both methods agree very well.

We have selected normally-distributed pseudo-random values for  $M_{dSN}^{(m)}$  (except for the first supernova, in which  $M_{dSN}^{(m)}$  was chosen so that  $Z_d = 10^{-3}$  at  $\tau_{inj}$ ) and  $\Delta\tau_{SN} = \tau_{SN}^{(m+1)} - \tau_{SN}^{(m)}$ ,

the interval between supernova events, with a mean  $0.5 M_{\odot}$  and standard deviation  $0.15 M_{\odot}$  for  $M_{dSN}^{(m)}$ ; and a mean interval between supernova explosions ( $\sim 17000$  yr for a  $10^5 M_{\odot}$  cluster, see Figure 1) obtained from the supernova rate output of Starburst99 synthesis model (Leitherer et al. 1999) with a standard Kroupa initial mass function with lower and upper cut-off masses  $0.1 M_{\odot}$  and  $100 M_{\odot}$ , respectively. The standard deviation for  $\Delta\tau_{SN}$  was taken to be 10% of the mean value.

These considerations, imply the presence of a time-dependent reservoir of dust grains embedded into the high-temperature ( $\sim 10^6$ - $10^7$  K) thermalized gas inside the star cluster volume.

We calculate the gas number density and temperature inside the star cluster by making use of our hydrodynamical model (thoroughly discussed in Silich et al. 2011; Palouš et al. 2013). Our models are quasi-adiabatic, however, they include the effects of gas (Raymond et al. 1976) and dust radiative cooling (Dwek 1987) (see Appendix A.1 for the complete description of the dust cooling calculation).

Once we know the conditions prevailing inside the star cluster volume (i.e. average values for the gas density and temperature), we can apply Dwek (1986) prescriptions to calculate the temperature distribution,  $G(a, T_d)$ , of dust grains which follow different dust size distributions. The infrared flux per unit wavelength, produced by a population of dust grains with the same chemical composition, from a star cluster located at distance  $D_{SC}$ , can then be calculated as (Dwek & Arendt 1992):

$$f_{\lambda} = \left( \frac{1.4m_H Z_d N_H}{\rho_d} \right) \pi \Omega_{SC} \int_{a_{min}}^{a_{max}} \int_0^{\infty} a^2 \frac{\partial n_i}{\partial a} Q_{abs}(\lambda, a) B_{\lambda}(T_d) G(a, T_d) dT_d da \quad (10)$$

in units  $\text{erg s}^{-1} \text{cm}^{-2} \text{\AA}^{-1}$ , or alternatively, in units  $\text{erg s}^{-1} \text{cm}^{-2} \text{Hz}^{-1}$  or Jansky, if one is interested in the flux per unit frequency,  $f_{\nu}$ , where  $\lambda f_{\lambda} = \nu f_{\nu}$ . Since both quantities,  $f_{\lambda}$  and  $f_{\nu}$ , are widely used by different authors (e.g. Reines et al. 2008; Adamo et al. 2010b; Fisher et al. 2014; Izotov et al. 2014), we present them both in all our figures, taking into account the contribution from graphite and silicate grains. In the above equation,  $N_H$  is the hydrogen column density through the star cluster volume ( $= 4/3nR_{SC}$ ),  $a$  is the dust grain radius,  $\rho_d = 4/3\pi\rho_{gr} \int_{a_{min}}^{a_{max}} a^3 \frac{\partial n_i}{\partial a} da$  is the size-averaged dust density, and  $\Omega_{SC} = \pi(R_{SC}/D_{SC})^2$ , is the solid angle subtended by the star cluster. Additionally,  $T_d$  is the dust temperature,  $G(a, T_d)$  is the dust temperature distribution resulting from stochastic temperature fluctuations,  $Q_{abs}(\lambda, a)$  is the dust absorption efficiency and  $B_{\lambda}(T_d)$  is the Planck function in terms of the wavelength,  $\lambda$ . In our models we have set the distance to the



star cluster as  $D_{SC} = 10$  Mpc. A complete discussion of the stochastic dust temperature fluctuations is presented in Appendix A.2.

In all our calculations, we neglected the charge of dust grains (Smith et al. 1996) as well as the contribution to the infrared flux from dust grains outside the star cluster volume. We are also not dealing with possible effects related to the absorption of ionizing photons by dust grains which could be important as long as the ionizing flux from the star cluster is strong. However, coeval clusters suffer a substantial reduction of their ionizing photon flux as soon as they enter the SN era. The number of emitted UV photons falls with time, as  $t^{-5}$  (Beltrametti et al. 1982) and thus after 5 – 6 Myr the number of UV photons is almost two orders of magnitude smaller than at the start of the evolution. This fall in the ionizing flux reduces the time during which the UV radiation may be more important than gas-dust collisions which could be important during all the type II SN era (from  $\sim 3$  to 40 Myr). The hydrodynamical model assumes that dust grains move with the same velocity as the injected gas and thus we have not considered the effects of kinetic sputtering in the intracluster medium.

### 3. Infrared Spectral Energy Distributions

To assess the impact that collisional heating of dust grains have on the expected infrared spectral energy distributions from young and massive dusty star clusters, we have run several models with the input parameters described in the previous section ( $L_{SC}$ ,  $V_{A\infty}$ ,  $R_c$ ,  $R_{SC}$ ,  $a_{min}$ ,  $a_{max}$  and  $t$ ). Our reference model *A*, consists of a star cluster with a total mass of  $10^5 M_{\odot}$  (which corresponds to a mechanical luminosity  $3 \times 10^{39}$  erg  $s^{-1}$ ),  $R_{hm} = 3.92$  pc (obtained from values  $R_c = 4$  pc and  $R_{SC} = 5$  pc), an adiabatic wind terminal speed  $V_{A\infty} = 1000$  km  $s^{-1}$ , lower and upper limits for the injected dust size distribution,  $a_{min} = 0.001 \mu\text{m}$  and  $a_{max} = 0.5 \mu\text{m}$ , respectively; and an equal mixture of graphite and silicate grains. The other models vary one or more of the input parameters with respect to model *A*. Models *B-C* explore different values of the mechanical luminosity, models *D* and *E* vary the adiabatic wind terminal speed and models *F* and *G* differ in the compactness of the star cluster. The reference model *A*, as well as models *B-G* are evaluated at the end of the first injection event ( $t = 1000$  yr) where, as pointed out before,  $M_{dSN}^{(1)}$  is set to allow  $Z_d(\tau_{inj})$  to be equal to  $10^{-3}$ . Models *A1-A4* are evaluated at later times. Table 2 presents the input parameters for our 11 models.

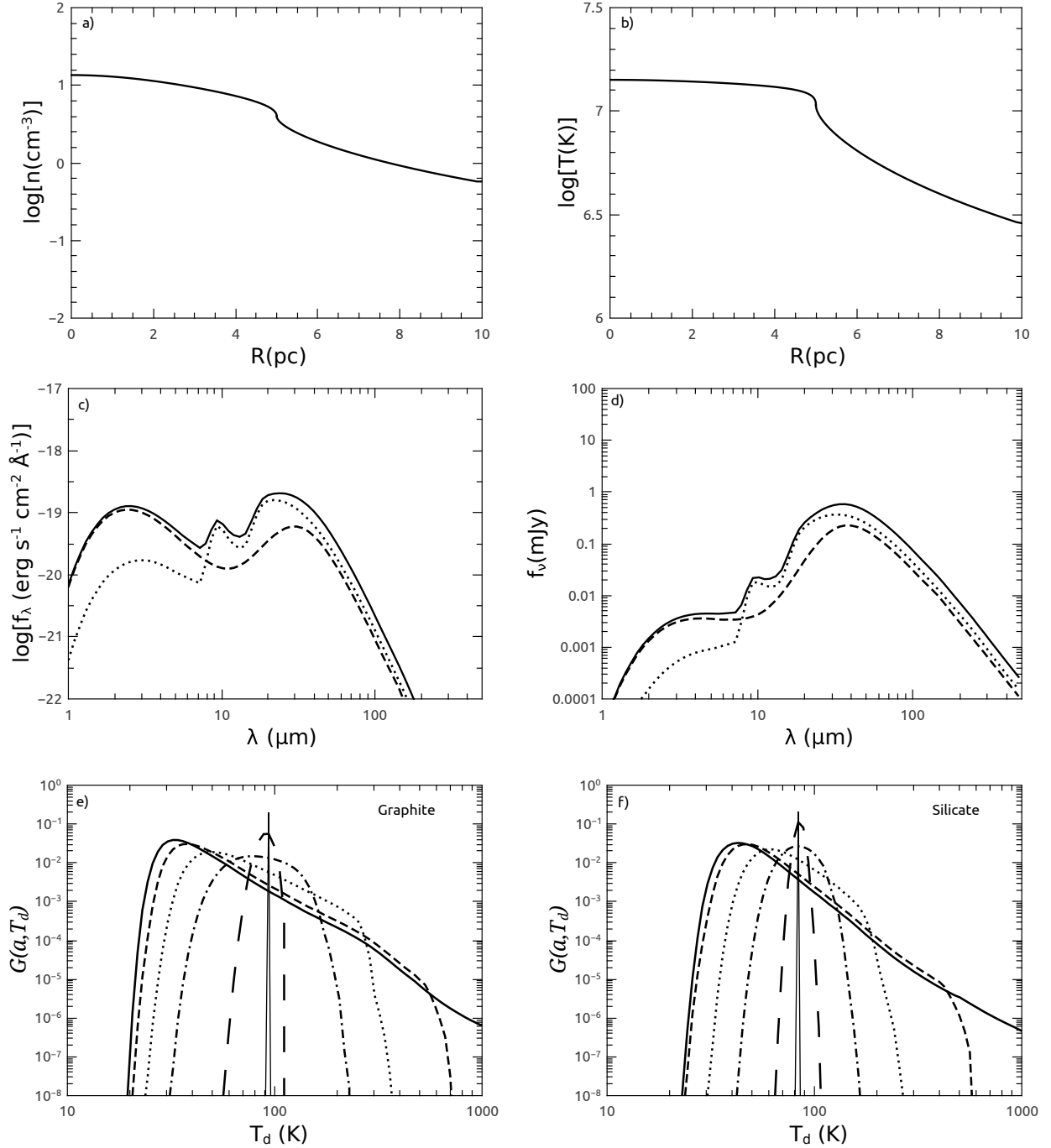


Fig. 2.— The Reference Model. Top panels a) and b), show the gas density and temperature radial profiles for our reference model *A*. Panels c) and d) present the fluxes per unit wavelength,  $f_\lambda$ , and per unit frequency,  $f_\nu$ , respectively. The dashed line depicts the contribution from graphite grains, the dotted line the contribution from silicate grains while the solid line comprises both contributions. Bottom panels e) and f), present the dust temperature distribution for different grain sizes for graphite and silicate grains, respectively. In the bottom panels, the solid, dashed, dotted, dashed-dotted, long-dashed and the delta-like curves correspond to sizes 0.001, 0.002, 0.01, 0.05, 0.1 and 0.5  $\mu\text{m}$ , respectively.

Table 2: Model Parameters

Model	t (yr)	$R_c$ (pc)	$R_{SC}$ (pc)	$R_{hm}$ (pc)	$L_{SC}$ (erg s <sup>-1</sup> )	$V_{A\infty}$ (km s <sup>-1</sup> )	$Z_d$ (10 <sup>-3</sup> )
<i>A</i>	1000	4	5	3.52	$3 \times 10^{39}$	1000	1.0
<i>A1</i>	17000	4	5	3.52	$3 \times 10^{39}$	1000	3.1
<i>A2</i>	17500	4	5	3.52	$3 \times 10^{39}$	1000	2.5
<i>A3</i>	25000	4	5	3.52	$3 \times 10^{39}$	1000	0.4
<i>A4</i>	33000	4	5	3.52	$3 \times 10^{39}$	1000	0.1
<i>B</i>	1000	4	5	3.52	$1 \times 10^{39}$	1000	1.0
<i>C</i>	1000	4	5	3.52	$9 \times 10^{39}$	1000	1.0
<i>D</i>	1000	4	5	3.52	$3 \times 10^{39}$	750	1.0
<i>E</i>	1000	4	5	3.52	$3 \times 10^{39}$	1500	1.0
<i>F</i>	1000	2	5	2.98	$3 \times 10^{39}$	1000	1.0
<i>G</i>	1000	4	7	4.59	$3 \times 10^{39}$	1000	1.0

### 3.1. The Reference Model

The outcomes from our reference model *A* are displayed in Figure 2. In this case, the prevailing conditions inside the star cluster are: an average value for the gas density  $\sim 10 \text{ cm}^{-3}$  and an average gas temperature  $\sim 1.35 \times 10^7 \text{ K}$ . From those conditions, we computed the dust temperature distributions,  $G(a, T_d)$ , for different dust sizes, and calculated the resultant flux averaged by the size distribution of graphite and silicate grains (see Appendix A.1). In order to quantify the contribution to the total flux, we display separate fluxes from graphite and from silicate grains. As shown in panels e) and f), small grains ( $\lesssim 0.05 \mu\text{m}$ ) are more likely to undergo strong temperature fluctuations and therefore span a wide range of temperatures (from a few  $\sim 10 \text{ K}$  to a few  $\sim 1000 \text{ K}$  for grains with  $a = 0.001 \mu\text{m}$ , making them to strongly emit in all near-infrared (NIR), mid-infrared (MIR) and far-infrared (FIR) wavelengths) due to their low heat capacities (which scale as  $\sim a^3$ ) and small cross sections.

Big grains ( $\gtrsim 0.1 \mu\text{m}$ ) with larger cross sections (which make them subject to more frequent collisions) emit nearly as a blackbody at their equilibrium temperature. Intermediate-size grains ( $0.05 \gtrsim a \gtrsim 0.1$ ) exhibit a combination of both behaviors. Hence, the emission from 1 to  $8 \mu\text{m}$  is dominated by hot and small graphite grains. Between 9 and  $14 \mu\text{m}$ , the emission is dominated by the 10-micron broad feature, associated to the dust absorption efficiency,  $Q_{abs}(\lambda, a)$ , of silicate grains. The emission from 15 to several hundred microns peaks around  $\sim 35 \mu\text{m}$ ; it is dominated by big grains near their equilibrium temperature ( $\sim 93 \text{ K}$  for graphite grains and  $\sim 75 \text{ K}$  for silicate grains) and by small grains with temperatures ranging from  $\sim 10 \text{ K}$  to  $\sim 100 \text{ K}$ . Note that the emission from graphite and silicate grains is almost

identical for  $\lambda \gtrsim 35 \mu\text{m}$  because their dust temperature distributions are very similar. In this case, the mass of dust inside the star cluster volume is  $M_d(t = \tau_{inj}) = 0.19 M_\odot$ .

We have evaluated our reference model *A* at four later times (models *A1*, *A2*, *A3* and *A4* evaluated at  $\sim 17000$ ,  $17500$ ,  $25000$ , and  $33000$  yr, respectively). When dust injection is not taking place (models *A2*-*A3*), the dust size distribution and the dust-to-gas mass ratio rapidly evolve and greatly depart from the injected dust size distribution as a consequence of the short timescale for thermal sputtering (see equation 4). This is reflected in a lack of small grains and therefore, the NIR excesses noted in models *A* and *A1* (evaluated just before the end of the first and second dust injection episodes, respectively) rapidly vanish. This situation is illustrated in Figure 3 which shows evolving spectral energy distributions for models *A*, *A1*, *A2*, *A3* and *A4*. Top panels show the evolution of the dust mass (panel a) and dust-to-gas mass ratio (panel b) during 9 injection events; the times at which these models were evaluated are marked with crosses. Bottom panels show evolving spectral energy distributions at the end of the first dust injection (1000 years, model *A*), at the end of the second dust injection. A strong emission at NIR and MIR wavelengths is present during dust injection, however, when dust injection has ceased, this strong emission rapidly vanishes which is notorious just 500 years after dust injection (model *A2*) due to the depletion of grains with radius  $\lesssim 0.01 \mu\text{m}$ . Models *A3* and *A4*, which are more affected by thermal sputtering and the exit of dust grains, have diminished dust-to-gas mass ratios and a negligible emission at NIR-MIR wavelengths.

If one compares flux ratios, e.g.  $f_\nu(25\mu\text{m})/f_\nu(100\mu\text{m})$  and  $f_\nu(3.5\mu\text{m})/f_\nu(25\mu\text{m})$ , one can note that the former is almost a constant around 10, while the latter rapidly approaches to zero. This is explained due to the fact that the emission at  $25 \mu\text{m}$  and  $100 \mu\text{m}$  originates mainly from big grains radiating at their equilibrium temperature (which are less affected by thermal sputtering), while the emission at  $3.5 \mu\text{m}$  comes from stochastically-heated small grains which are strongly affected by thermal sputtering. The mass of dust in models *A1*-*A4* is  $0.61$ ,  $0.51$ ,  $0.14$  and  $0.06 M_\odot$ , respectively. We note that in these models, roughly 20% of the total mass injected by each supernova explosion is expelled out from the star cluster as a wind.

### 3.2. Models with Different Star Cluster Mechanical Luminosities

The results derived from models *A*, *B* and *C* are shown in Figure 4. These models (as well as models *D*-*G*) are evaluated at  $t = \tau_{inj} = 1000$  yr. Models *B* and *C* consider three times smaller ( $L_{SC} = 1 \times 10^{39} \text{ erg s}^{-1}$ ) and three times larger ( $L_{SC} = 9 \times 10^{39} \text{ erg s}^{-1}$ ) values of the star cluster mechanical luminosity than what is considered in model *A*, respectively.

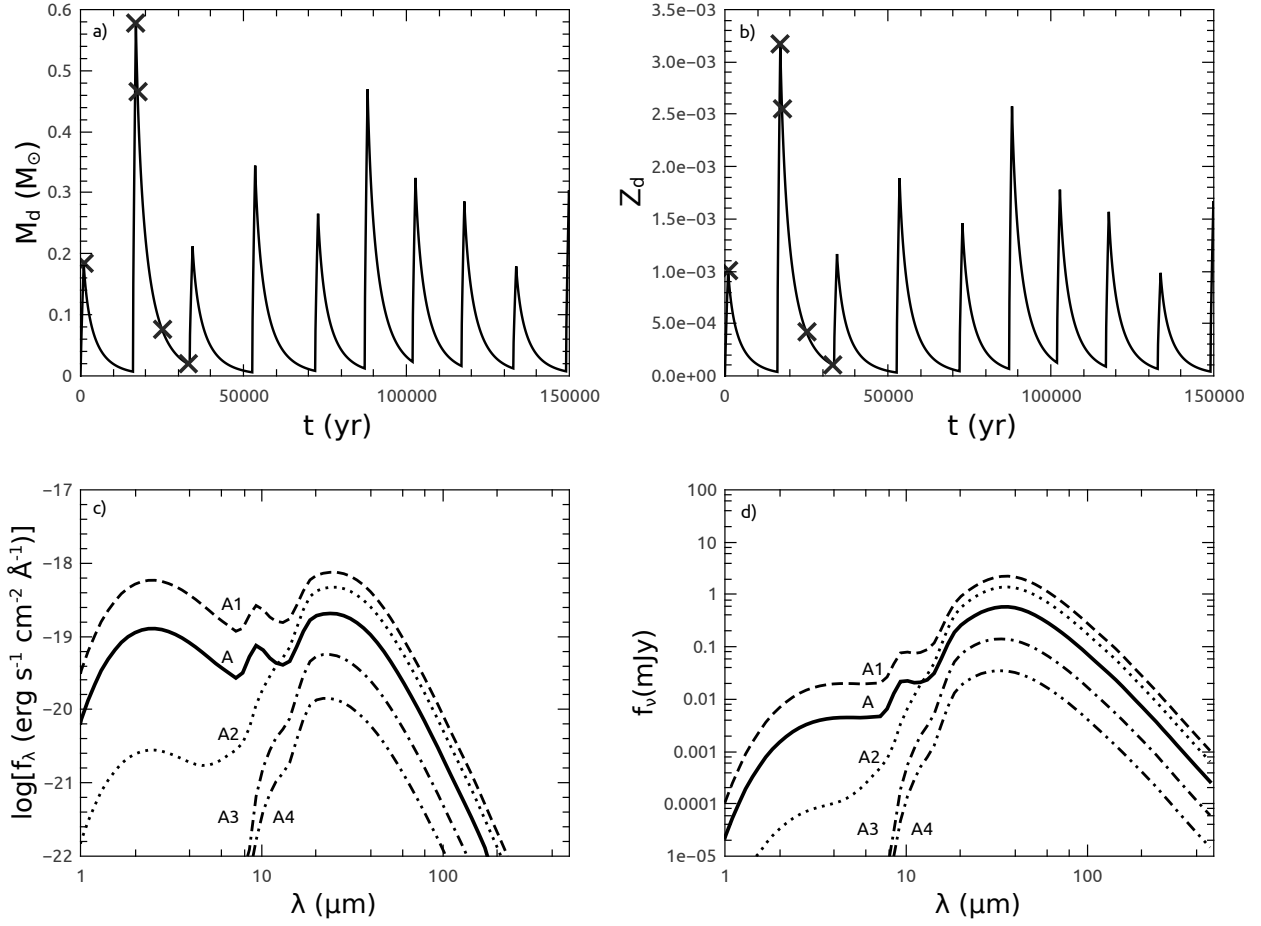


Fig. 3.— Spectral Energy Distributions for models  $A$ ,  $A1$ ,  $A2$ ,  $A3$  and  $A4$ . Top panels a) and b) show the evolution of the dust mass and dust-to-gas mass ratio, respectively, during 9 injection events taking into account both dust sputtering and their exit out of the cluster as a wind. The times at which models  $A1$ - $A4$  were evaluated are marked with crosses. Bottom panels c) and d) present the values of the fluxes per unit wavelength,  $f_\lambda$ , and per unit frequency,  $f_\nu$ , for each evolved models, respectively. Solid, dashed, dotted, dashed-dotted and dashed-double-dotted lines depict the SEDs for models  $A$ ,  $A1$ ,  $A2$ ,  $A3$  and  $A4$ , respectively. Note that the strong emission present during dust injection rapidly vanishes when dust injection has ceased.

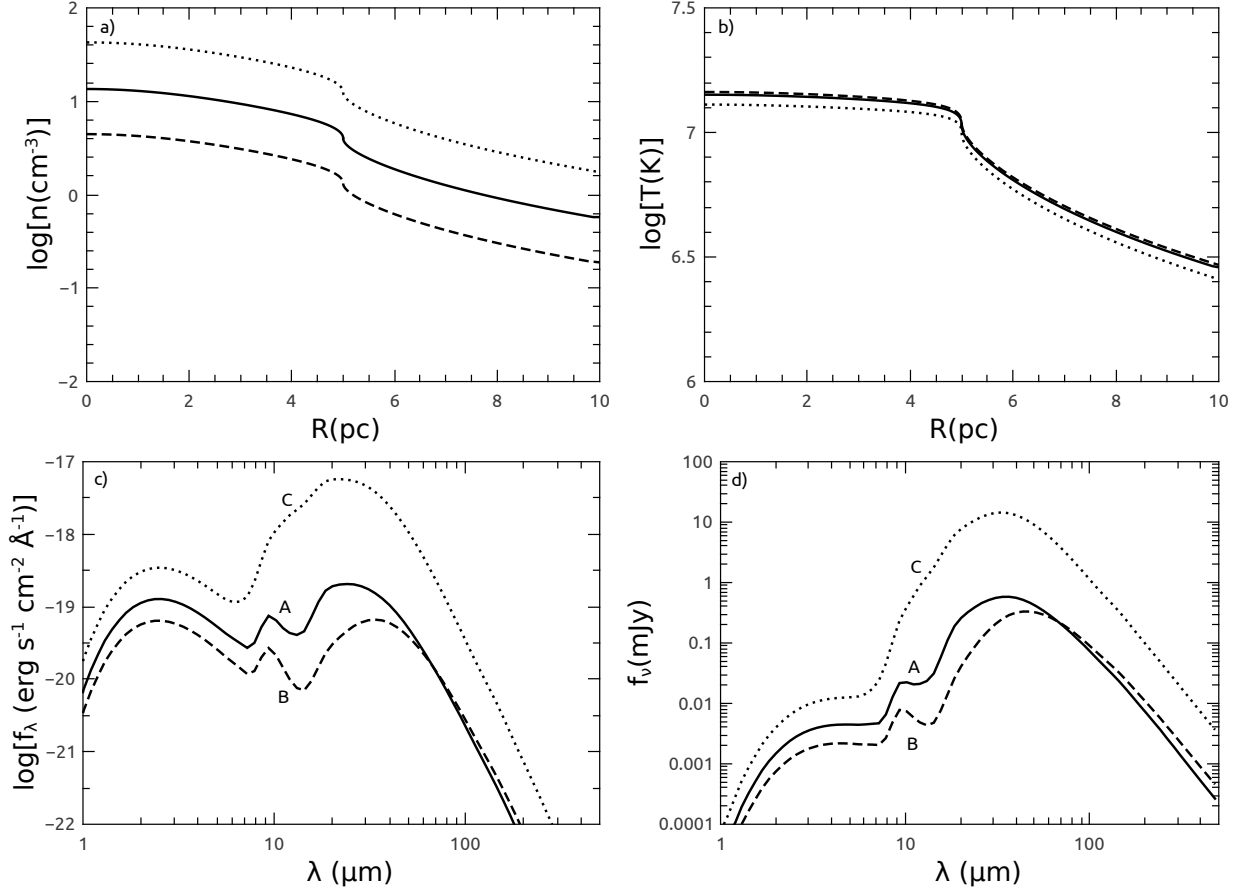


Fig. 4.— Results for models with different mechanical luminosities  $A$  ( $3 \times 10^{39}$  erg  $\text{s}^{-1}$ , solid curves),  $B$  ( $1 \times 10^{39}$  erg  $\text{s}^{-1}$ , dashed curves) and  $C$  ( $9 \times 10^{39}$  erg  $\text{s}^{-1}$ , dotted curves). Panels a) and b) show the gas number density and temperature profiles of each model, respectively. Panels c) and d) present the values of the fluxes per unit wavelength,  $f_\lambda$ , and per unit frequency,  $f_\nu$ , for each model, respectively. Note that an increase in the star cluster mechanical luminosity (or equivalently in the mass of the star cluster), leads to an increase in the infrared emission from dust grains.

An increase in the value of  $L_{SC}$ , yields a higher gas density inside the star cluster, which results in more frequent gas-grain collisions leading to an increase in the infrared emission (see equations A11 and A13 in Appendix A.2). As more massive clusters are considered, a higher supernova rate is expected and therefore, there is less time between supernova episodes to erode dust grains. This leads to a more persistent dust reservoir at all times which is reflected in an enhancement of the infrared spectrum. Thus, model  $C$  surpasses the infrared emission from models  $A$  and  $B$ . However, model  $C$  is also more affected by thermal sputtering which is noticeable by a decreased emission at  $\lambda \lesssim 15 \mu\text{m}$ . The mass of dust inside  $R_{SC}$  at  $t = \tau_{inj}$  is  $6.0 \times 10^{-2} M_{\odot}$  and  $0.57 M_{\odot}$  for models  $B$  and  $C$ , respectively.

### 3.3. Models with Different Adiabatic Terminal Speeds

Figure 5 shows the results obtained from models  $A, G$  and  $E$ . In these models we examine different values of the adiabatic wind terminal speed. As the gas density decreases with an increasing adiabatic wind terminal speed, the characteristic time between successive electron collisions with a dust grain increases (see equation A11 in Appendix A.2). Dust grains then are less heated and their emission decreases (model  $E$  compared to model  $A$ ). The opposite situation occurs in models with a lower value of the adiabatic wind terminal speed (model  $D$  compared to model  $A$ ) which also causes a decreased in the emission at  $\lambda \lesssim 15 \mu\text{m}$  provoked by the depletion of small grains by the action of thermal sputtering in a denser medium. The mass of dust inside  $R_{SC}$  is  $0.47 M_{\odot}$  and  $5.29 \times 10^{-2} M_{\odot}$  for models  $D$  and  $E$ , respectively.

### 3.4. Models for Different Cluster Sizes

We now focus on models with different values of  $R_c$  and  $R_{SC}$  (see Figure 6). Model  $F$  is evaluated with a smaller star cluster core radius  $R_c = 2 \text{ pc}$ . Model  $G$  corresponds to a star cluster with a larger cut-off radius  $R_{SC} = 7 \text{ pc}$ . A more compact cluster, as in model  $F$  compared to model  $A$ , yields an enhanced flux at all wavelengths, however, this effect is more noticeable at FIR wavelengths where the role of thermal sputtering is less important. The situation is different when one considers a less compact cluster (model  $G$  compared to model  $A$ ), when the gas number density is decreased and therefore, the dust emission is diminished. In these models, half of the star cluster mass is located inside  $3.52 \text{ pc}$ ,  $2.98 \text{ pc}$  and  $4.59 \text{ pc}$  for models  $A$ ,  $F$  and  $G$ , respectively. The mass of dust inside the star cluster volume is  $0.21 M_{\odot}$  and  $8.62 \times 10^{-2} M_{\odot}$  for models  $F$  and  $G$ , respectively.

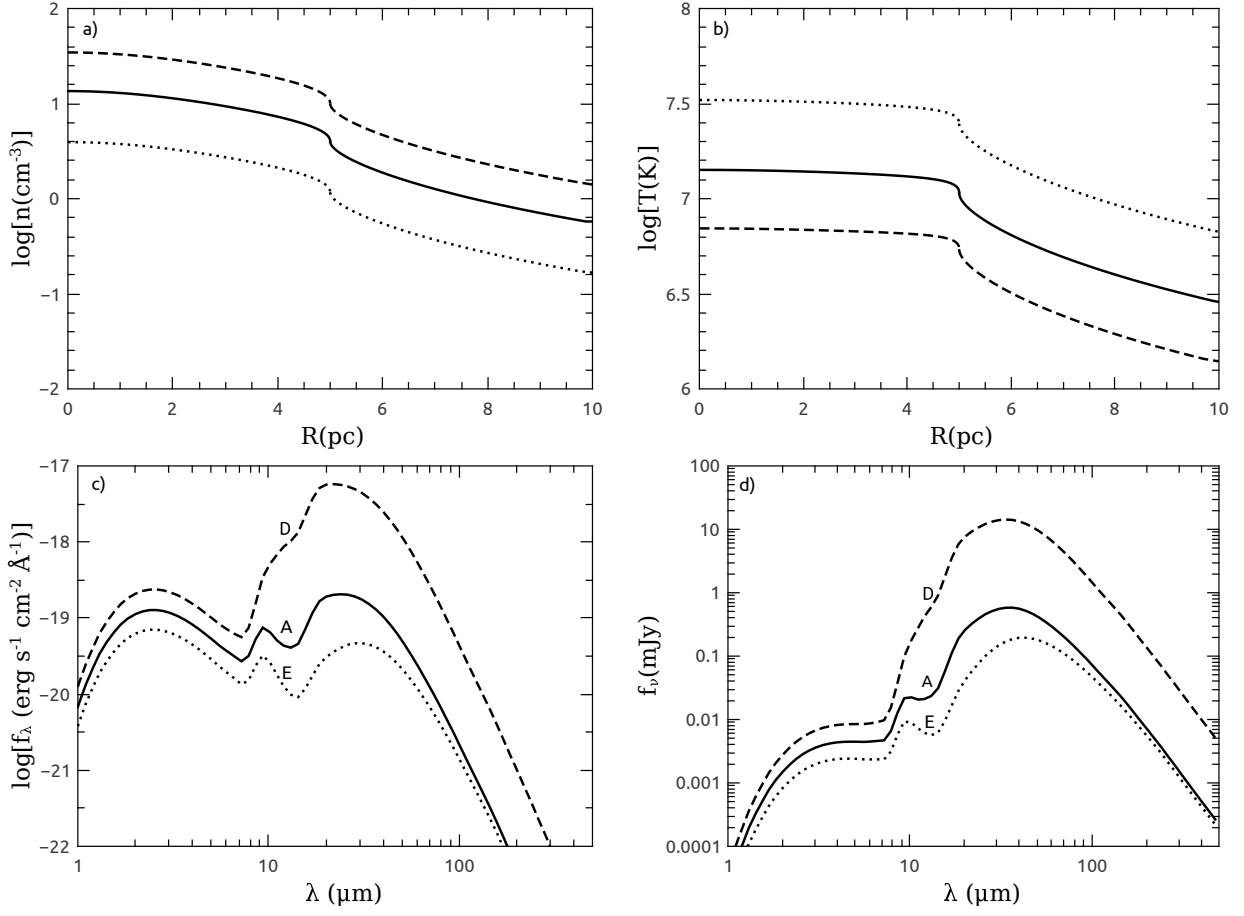


Fig. 5.— Same as Figure 4 but for models with different adiabatic wind terminal speeds  $A$  ( $1000 \text{ km s}^{-1}$ , solid curves),  $D$  ( $750 \text{ km s}^{-1}$ , dashed curves) and  $E$  ( $1500 \text{ km s}^{-1}$ , dotted curves). Note that an increase in the adiabatic terminal speed, lead to a decrease in the dust emission inside the star cluster volume.



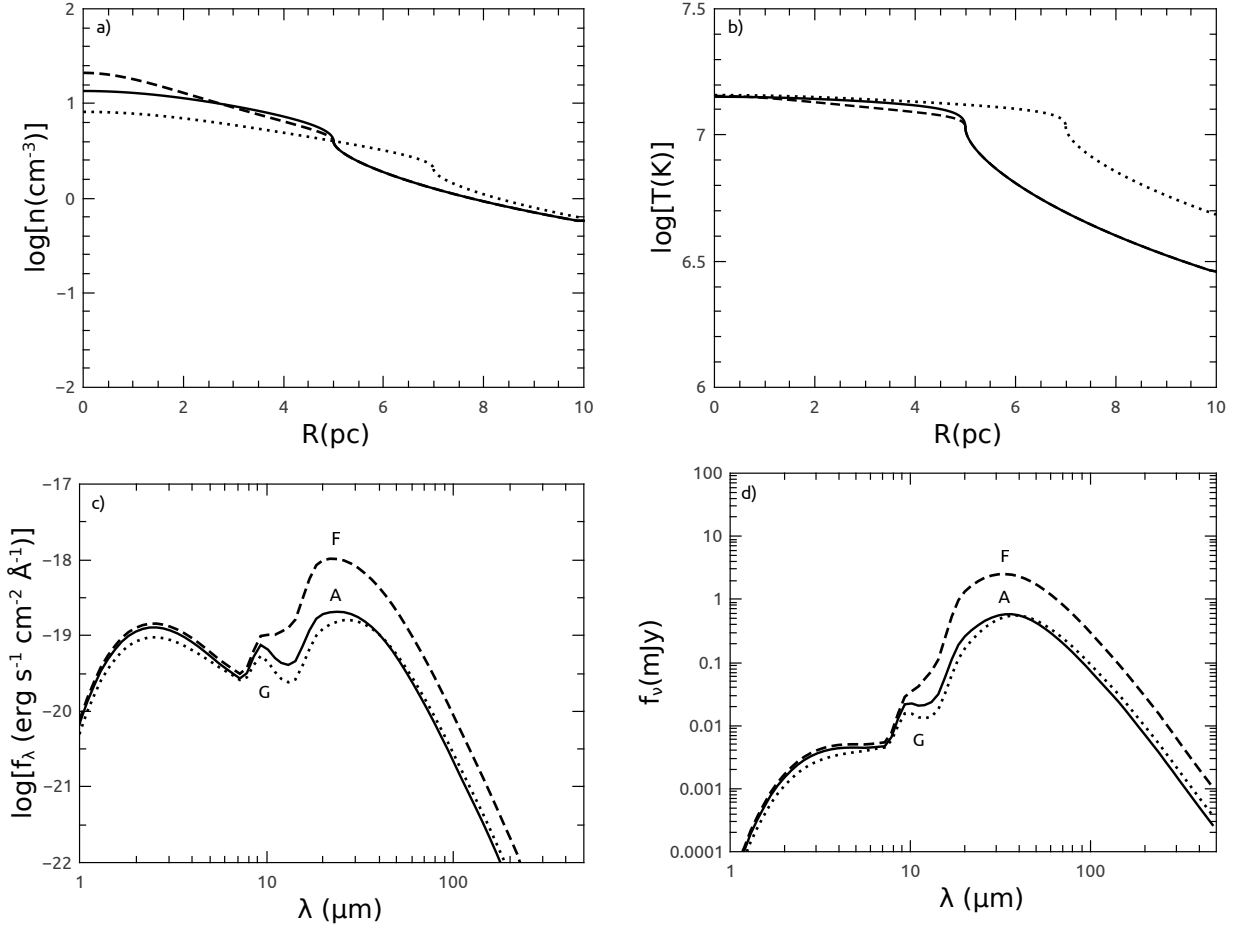


Fig. 6.— Same as Figure 4 but for models with different star cluster sizes. Solid lines correspond to model *A* ( $R_c = 4$  pc,  $R_{SC} = 5$  pc and  $R_{hm} = 3.92$  pc), dashed lines display the results obtained from model *F* ( $R_c = 2$  pc,  $R_{SC} = 5$  pc and  $R_{hm} = 3.52$  pc), and dotted lines show the results from model *G* ( $R_c = 4$  pc,  $R_{SC} = 7$  pc and  $R_{hm} = 5.45$  pc). Note that more compact clusters lead to an increase in the dust emission inside the star cluster volume, especially at FIR wavelengths.

## 4. Conclusions

Motivated by the abundant evidence for core-collapse supernovae as major dust producers, and the large SN rate expected in young massive star clusters, we have studied the frequent injection of dust grains into the plasma interior of super star clusters, which become ideal places to heat dust grains by means of random gas-grain collisions. This has led us to combine our hydrodynamic star cluster wind model with the stochastic dust injection, heating and cooling models to calculate the expected spectral energy distributions from super stellar clusters.

We have followed the evolution of the grain size distribution, what changes drastically, the resultant spectrum. We have also considered the exit of dust grains as they stream out, coupled to the gas, to compose the star cluster wind. For the latter, we have used a finite difference method.

In this scenario, a certain mass of silicate and graphite dust, and an initial grain size distribution is injected into the intracluster medium. On top of this, the stellar winds are steady but the rate of supernova makes the dust injection an stochastic process. Therefore, dust is injected into the medium stochastically, and then heated and eroded before the next injection episode.

Several models were defined in order to quantify all these effects in the resultant infrared spectrum. Models which give more weight in the dust size distribution to small grains (as when dust injection is taking place), as well as models with larger values of the star cluster mechanical luminosity (in which the SN rate increases leading to more persistent dust reservoirs), lead to an enhanced dust emission. The opposite situation occurs with more extended star clusters and larger adiabatic terminal speeds, which lead to a decrease in their dust emission. When dust injection ceases, the resultant SEDs change drastically and the emission at NIR-MIR wavelengths vanishes due to thermal sputtering acting more effectively on small grains.

Despite the fact that our models imply the presence from hundredths to tenths of solar masses of dust inside the star cluster volume and transient strong NIR-MIR infrared excesses, the predicted SEDs are strong enough to be considered in order to explain the infrared excesses observed in bright young clusters and other stellar systems. In those cases, the combined action of many nearby star clusters, as well as higher SN rates in more massive clusters, could led to persistent infrared excesses. This and a detailed comparison with the observations of starburst galaxies will be addressed in a forthcoming communication.

## 5. Acknowledgements

We thank our anonymous referee for a detailed report full of valuable comments and helpful suggestions which greatly improved the paper. This study has been supported by CONACYT - México, research grants 167169, and 131913 and by the Spanish Ministry of Science and Innovation under the collaboration ESTALLIDOS (grants AYA2010-21887-C04-04 estallidosIV and AYA2013-47742-C4-2-P estallidos5). GTT also acknowledges the Cátedra Severo Ochoa at the Instituto de Astrofísica de Canarias (IAC, Tenerife Spain) and the CONACYT grant 232876 for a sabbatical leave. SMG acknowledges Prof. B. T. Draine for his comments which helped to understand the normalization of the dust size distributions.

### A. Appendix

#### A.1. The Cooling Function via Gas-Grain Collisions

Following Dwek (1987), and keeping most of his notations and definitions, we calculated the cooling rate due to the gas-grain collisions in a dusty plasma with a normal chemical composition (one He atom per every ten H atoms):

$$\Lambda_d = \frac{n_d}{n_e n} H_{coll} = \frac{1.4 m_H Z_d}{\rho_d} \left( \frac{32}{\pi m_e} \right)^{1/2} \pi (k_B T)^{3/2} \left[ h_e + \frac{11}{23} \left( \frac{m_e}{m_H} \right)^{1/2} h_n \right], \quad (\text{A1})$$

where  $n$ ,  $n_d$  and  $n_e$  are the gas, dust and electron number density,  $H_{coll}$  is the heating rate of a single grain due to collisions with incident gas particles and  $k_B$  is the Boltzmann constant. Functions  $h_e$  and  $h_H$  are the effective grain heating efficiencies due to impinging electrons and nuclei, respectively:

$$h_e = \int_{a_{min}}^{a_{max}} \int_0^\infty \frac{\zeta(a, E)}{2} x_e^2 e^{-x_e} a^2 \frac{\partial n_i}{\partial a} dx_e da, \quad (\text{A2})$$

$$h_n = \int_{a_{min}}^{a_{max}} \left\{ \left[ 1 - \left( 1 + \frac{x_H}{2} \right) e^{-x_H} \right] + \frac{1}{2} \left[ 1 - \left( 1 + \frac{x_{He}}{2} \right) e^{-x_{He}} \right] \right\} a^2 \frac{\partial n_i}{\partial a} da, \quad (\text{A3})$$

where  $\rho_d = 4/3\pi\rho_{gr} \int_{a_{min}}^{a_{max}} a^3 \frac{\partial n_i}{\partial a} da$  is the size-averaged dust density,  $\rho_{gr}$  is the grain density,  $x_e = E/k_B T$ ,  $E$  is the energy of the impinging electron,  $\zeta(a, E)$  is the fraction of the electron kinetic energy transferred to the dust grain,  $x_H = E_H/k_B T$ ,  $x_{He} = E_{He}/k_B T$  and the energies from the incident hydrogen and helium nuclei are  $E_H = 133a$  keV,  $E_{He} = 222a$  keV, where  $a$  is measured in microns,

$$\zeta(a, E) = \begin{cases} 0.875, & \text{if } E \leq E^* \\ 1 - E_f/E, & \text{otherwise,} \end{cases} \quad (\text{A4})$$

where  $E_f = \max\{E', 0.125E\}$ , with  $E^*$  and  $E'$ , the critical energy at which an electron penetrates the dust grain and the final energy of the electron after penetrating the dust grain, respectively.  $E^*$  and  $E'$  are obtained by solving the following system of non-linear equations based on experimental data

$$\log R(E^*) = \log(4a\rho_{gr}/3) = 0.146 \log E^{*2} + 0.5 \log E^* - 8.15, \quad (\text{A5})$$

$$\log R(E) = 0.146 \log E^2 + 0.5 \log E - 8.15, \quad (\text{A6})$$

$$\log R(E') = \log R(E) - R(E^*) = 0.146 \log E'^2 + 0.5 \log E' - 8.15. \quad (\text{A7})$$

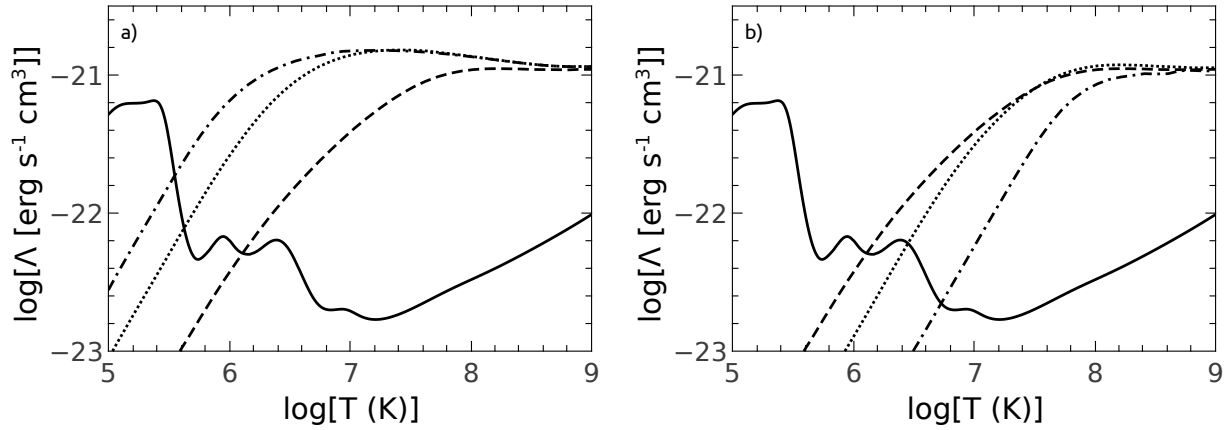


Fig. 7.— Cooling function for different MRN dust size distributions as a function of temperature. In panel a),  $a_{min}$  is set to  $0.001 \mu\text{m}$  and  $a_{max}$  takes the values  $0.001$ ,  $0.01$  and  $0.5 \mu\text{m}$  (dashed, dotted, and dash-dotted lines, respectively). In panel b),  $a_{max}$  is set to  $0.5 \mu\text{m}$  and  $a_{min}$  takes the values  $0.001$ ,  $0.01$  and  $0.5 \mu\text{m}$  (dashed, dotted, and dash-dotted lines, respectively). In these calculations, we assumed a dust-to-gas mass ratio of  $Z_d = 10^{-3}$ . In both panels, the interstellar cooling law for solar metallicity is presented as a solid curve.

In Figure 7, we show examples of the dust cooling curves for different cases of the MRN dust size distributions in which the value of the dust-to-gas mass ratio is set to  $Z_d = 10^{-3}$ . Finally, we provide tables which contain the results of the calculations of the dust cooling function for different MRN dust size distributions as a function of the gas temperature and normalized to the dust-to-gas mass ratio, for  $a_{min}$  set to  $0.001 \mu\text{m}$  and different  $a_{max}$  values (Table 3), and for  $a_{max}$  set to  $0.5 \mu\text{m}$  and different  $a_{min}$  values (Table 4).

Table 3: The Cooling Function with different MRN dust size distribution (with  $a_{min} = 0.001$   $\mu\text{m}$  in all cases) normalized to the dust-to-gas mass ratio.

$a_{max}$ ( $\mu\text{m}$ )	0.001	0.002	0.005	0.01	0.05	0.1	0.5
T (K)	$\Lambda_d/Z_d$ ( $\text{erg s}^{-1} \text{cm}^3$ )						
1.00E+04	8.787E-22	6.213E-22	3.930E-22	2.778E-22	1.234E-22	8.606E-23	3.565E-23
1.25E+04	1.256E-21	8.884E-22	5.619E-22	3.973E-22	1.774E-22	1.252E-22	5.702E-23
1.57E+04	1.763E-21	1.246E-21	7.883E-22	5.574E-22	2.490E-22	1.756E-22	8.000E-23
1.97E+04	2.473E-21	1.749E-21	1.106E-21	7.821E-22	3.493E-22	2.464E-22	1.122E-22
2.47E+04	3.470E-21	2.453E-21	1.552E-21	1.097E-21	4.900E-22	3.457E-22	1.575E-22
3.09E+04	4.868E-21	3.442E-21	2.177E-21	1.539E-21	6.875E-22	4.850E-22	2.209E-22
3.87E+04	6.830E-21	4.830E-21	3.054E-21	2.160E-21	9.646E-22	6.805E-22	3.100E-22
4.86E+04	9.583E-21	6.776E-21	4.286E-21	3.030E-21	1.353E-21	9.547E-22	4.349E-22
6.09E+04	1.344E-20	9.507E-21	6.013E-21	4.251E-21	1.899E-21	1.339E-21	6.102E-22
7.63E+04	1.886E-20	1.334E-20	8.436E-21	5.965E-21	2.664E-21	1.879E-21	8.561E-22
9.56E+04	2.646E-20	1.871E-20	1.184E-20	8.369E-21	3.737E-21	2.637E-21	1.201E-21
1.20E+05	3.713E-20	2.625E-20	1.660E-20	1.174E-20	5.244E-21	3.699E-21	1.685E-21
1.50E+05	5.209E-20	3.683E-20	2.330E-20	1.647E-20	7.357E-21	5.190E-21	2.364E-21
1.88E+05	7.308E-20	5.168E-20	3.269E-20	2.311E-20	1.032E-20	7.282E-21	3.317E-21
2.36E+05	1.025E-19	7.250E-20	4.586E-20	3.242E-20	1.448E-20	1.022E-20	4.653E-21
2.96E+05	1.434E-19	1.017E-19	6.431E-20	4.548E-20	2.031E-20	1.433E-20	6.524E-21
3.70E+05	1.995E-19	1.422E-19	9.010E-20	6.373E-20	2.847E-20	2.008E-20	9.132E-21
4.64E+05	2.737E-19	1.978E-19	1.258E-19	8.907E-20	3.981E-20	2.807E-20	1.274E-20
5.82E+05	3.672E-19	2.716E-19	1.744E-19	1.238E-19	5.540E-20	3.907E-20	1.767E-20
7.29E+05	4.773E-19	3.651E-19	2.389E-19	1.703E-19	7.650E-20	5.395E-20	2.428E-20
9.14E+05	5.998E-19	4.772E-19	3.213E-19	2.310E-19	1.045E-19	7.370E-20	3.300E-20
1.15E+06	7.272E-19	6.032E-19	4.223E-19	3.077E-19	1.406E-19	9.932E-20	4.426E-20
1.44E+06	8.536E-19	7.363E-19	5.399E-19	4.012E-19	1.863E-19	1.319E-19	5.851E-20
1.80E+06	9.735E-19	8.691E-19	6.701E-19	5.109E-19	2.428E-19	1.724E-19	7.629E-20
2.25E+06	1.080E-18	9.951E-19	8.063E-19	6.342E-19	3.111E-19	2.218E-19	9.808E-20
2.82E+06	1.176E-18	1.110E-18	9.415E-19	7.667E-19	3.918E-19	2.810E-19	1.244E-19
3.54E+06	1.264E-18	1.209E-18	1.068E-18	9.016E-19	4.850E-19	3.508E-19	1.561E-19
4.44E+06	1.329E-18	1.296E-18	1.183E-18	1.033E-18	5.902E-19	4.316E-19	1.933E-19
5.56E+06	1.383E-18	1.365E-18	1.280E-18	1.153E-18	7.051E-19	5.232E-19	2.371E-19
6.97E+06	1.447E-18	1.419E-18	1.360E-18	1.258E-18	8.264E-19	6.248E-19	2.879E-19
8.73E+06	1.485E-18	1.469E-18	1.425E-18	1.346E-18	9.494E-19	7.345E-19	3.459E-19
1.09E+07	1.498E-18	1.508E-18	1.473E-18	1.415E-18	1.067E-18	8.484E-19	4.117E-19
1.37E+07	1.506E-18	1.522E-18	1.505E-18	1.465E-18	1.174E-18	9.614E-19	4.849E-19
1.72E+07	1.508E-18	1.520E-18	1.523E-18	1.497E-18	1.265E-18	1.068E-18	5.646E-19
2.15E+07	1.505E-18	1.514E-18	1.532E-18	1.516E-18	1.336E-18	1.161E-18	6.494E-19
2.70E+07	1.497E-18	1.503E-18	1.524E-18	1.518E-18	1.387E-18	1.238E-18	7.367E-19
3.38E+07	1.483E-18	1.488E-18	1.502E-18	1.514E-18	1.419E-18	1.297E-18	8.224E-19
4.24E+07	1.464E-18	1.468E-18	1.478E-18	1.496E-18	1.434E-18	1.336E-18	9.022E-19
5.31E+07	1.441E-18	1.444E-18	1.451E-18	1.463E-18	1.434E-18	1.357E-18	9.716E-19
6.66E+07	1.414E-18	1.416E-18	1.421E-18	1.429E-18	1.422E-18	1.363E-18	1.027E-18
8.35E+07	1.384E-18	1.385E-18	1.389E-18	1.394E-18	1.400E-18	1.356E-18	1.068E-18
1.05E+08	1.352E-18	1.353E-18	1.355E-18	1.359E-18	1.375E-18	1.340E-18	1.095E-18
1.31E+08	1.319E-18	1.319E-18	1.321E-18	1.324E-18	1.339E-18	1.315E-18	1.109E-18
1.64E+08	1.286E-18	1.286E-18	1.287E-18	1.289E-18	1.295E-18	1.290E-18	1.113E-18
2.06E+08	1.253E-18	1.254E-18	1.254E-18	1.256E-18	1.258E-18	1.257E-18	1.110E-18
2.58E+08	1.224E-18	1.224E-18	1.224E-18	1.225E-18	1.225E-18	1.219E-18	1.106E-18
3.23E+08	1.197E-18	1.197E-18	1.198E-18	1.198E-18	1.197E-18	1.190E-18	1.097E-18
4.05E+08	1.176E-18	1.176E-18	1.176E-18	1.176E-18	1.175E-18	1.167E-18	1.095E-18
5.08E+08	1.160E-18	1.160E-18	1.160E-18	1.160E-18	1.159E-18	1.153E-18	1.094E-18
6.37E+08	1.151E-18	1.152E-18	1.152E-18	1.152E-18	1.151E-18	1.145E-18	1.090E-18
7.98E+08	1.151E-18	1.151E-18	1.151E-18	1.152E-18	1.151E-18	1.147E-18	1.099E-18

Table 4: The Cooling Function with different MRN dust size distribution (with  $a_{max} = 0.5 \mu\text{m}$  in all cases) normalized to the dust-to-gas mass ratio.

$a_{min}$ ( $\mu\text{m}$ )	0.001	0.002	0.005	0.01	0.05	0.1	0.5
T (K)	$\Lambda_d/Z_d$ ( $\text{erg s}^{-1} \text{cm}^3$ )						
1.00E+04	3.565E-23	2.625E-23	1.721E-23	1.234E-23	5.556E-24	3.930E-24	1.757E-24
1.25E+04	5.702E-23	3.959E-23	2.504E-23	1.774E-23	7.946E-24	5.619E-24	2.513E-24
1.57E+04	8.000E-23	5.555E-23	3.513E-23	2.489E-23	1.115E-23	7.883E-24	3.525E-24
1.97E+04	1.122E-22	7.794E-23	4.928E-23	3.493E-23	1.564E-23	1.106E-23	4.946E-24
2.47E+04	1.575E-22	1.093E-22	6.914E-23	4.900E-23	2.195E-23	1.552E-23	6.940E-24
3.09E+04	2.209E-22	1.534E-22	9.701E-23	6.875E-23	3.079E-23	2.177E-23	9.736E-24
3.87E+04	3.100E-22	2.152E-22	1.361E-22	9.646E-23	4.320E-23	3.055E-23	1.366E-23
4.86E+04	4.349E-22	3.020E-22	1.910E-22	1.353E-22	6.061E-23	4.286E-23	1.917E-23
6.09E+04	6.102E-22	4.237E-22	2.679E-22	1.899E-22	8.503E-23	6.012E-23	2.689E-23
7.63E+04	8.561E-22	5.944E-22	3.759E-22	2.664E-22	1.193E-22	8.436E-23	3.773E-23
9.56E+04	1.201E-21	8.340E-22	5.273E-22	3.738E-22	1.674E-22	1.183E-22	5.293E-23
1.20E+05	1.685E-21	1.170E-21	7.399E-22	5.244E-22	2.348E-22	1.661E-22	7.426E-23
1.50E+05	2.364E-21	1.642E-21	1.038E-21	7.357E-22	3.295E-22	2.330E-22	1.042E-22
1.88E+05	3.317E-21	2.303E-21	1.456E-21	1.032E-21	4.622E-22	3.268E-22	1.462E-22
2.36E+05	4.653E-21	3.231E-21	2.043E-21	1.448E-21	6.485E-22	4.586E-22	2.051E-22
2.96E+05	6.524E-21	4.533E-21	2.867E-21	2.032E-21	9.099E-22	6.434E-22	2.877E-22
3.70E+05	9.132E-21	6.360E-21	4.022E-21	2.851E-21	1.276E-21	9.027E-22	4.037E-22
4.64E+05	1.274E-20	8.922E-21	5.643E-21	3.999E-21	1.791E-21	1.266E-21	5.664E-22
5.82E+05	1.767E-20	1.251E-20	7.917E-21	5.611E-21	2.513E-21	1.777E-21	7.946E-22
7.29E+05	2.428E-20	1.751E-20	1.111E-20	7.872E-21	3.525E-21	2.493E-21	1.115E-21
9.14E+05	3.300E-20	2.441E-20	1.558E-20	1.105E-20	4.946E-21	3.497E-21	1.564E-21
1.15E+06	4.426E-20	3.380E-20	2.185E-20	1.550E-20	6.940E-21	4.907E-21	2.195E-21
1.44E+06	5.851E-20	4.632E-20	3.060E-20	2.174E-20	9.736E-21	6.885E-21	3.079E-21
1.80E+06	7.629E-20	6.266E-20	4.270E-20	3.049E-20	1.366E-20	9.659E-21	4.320E-21
2.25E+06	9.808E-20	8.350E-20	5.918E-20	4.271E-20	1.916E-20	1.355E-20	6.061E-21
2.82E+06	1.244E-19	1.095E-19	8.113E-20	5.963E-20	2.689E-20	1.901E-20	8.503E-21
3.54E+06	1.561E-19	1.413E-19	1.097E-19	8.271E-20	3.772E-20	2.668E-20	1.193E-20
4.44E+06	1.933E-19	1.796E-19	1.458E-19	1.135E-19	5.292E-20	3.743E-20	1.674E-20
5.56E+06	2.371E-19	2.251E-19	1.903E-19	1.534E-19	7.420E-20	5.251E-20	2.348E-20
6.97E+06	2.879E-19	2.782E-19	2.439E-19	2.036E-19	1.038E-19	7.366E-20	3.295E-20
8.73E+06	3.459E-19	3.394E-19	3.071E-19	2.649E-19	1.444E-19	1.032E-19	4.622E-20
1.09E+07	4.117E-19	4.088E-19	3.799E-19	3.376E-19	1.988E-19	1.443E-19	6.485E-20
1.37E+07	4.849E-19	4.865E-19	4.621E-19	4.214E-19	2.691E-19	2.001E-19	9.098E-20
1.72E+07	5.646E-19	5.716E-19	5.527E-19	5.152E-19	3.561E-19	2.736E-19	1.276E-19
2.15E+07	6.494E-19	6.621E-19	6.495E-19	6.166E-19	4.583E-19	3.659E-19	1.783E-19
2.70E+07	7.367E-19	7.551E-19	7.499E-19	7.223E-19	5.719E-19	4.746E-19	2.470E-19
3.38E+07	8.224E-19	8.465E-19	8.491E-19	8.266E-19	6.905E-19	5.940E-19	3.354E-19
4.24E+07	9.022E-19	9.315E-19	9.413E-19	9.247E-19	8.060E-19	7.157E-19	4.413E-19
5.31E+07	9.716E-19	1.005E-18	1.021E-18	1.011E-18	9.110E-19	8.300E-19	5.572E-19
6.66E+07	1.027E-18	1.064E-18	1.086E-18	1.081E-18	9.989E-19	9.287E-19	6.724E-19
8.35E+07	1.068E-18	1.107E-18	1.132E-18	1.132E-18	1.067E-18	1.008E-18	7.781E-19
1.05E+08	1.095E-18	1.135E-18	1.162E-18	1.165E-18	1.113E-18	1.065E-18	8.625E-19
1.31E+08	1.109E-18	1.149E-18	1.177E-18	1.182E-18	1.144E-18	1.103E-18	9.281E-19
1.64E+08	1.113E-18	1.152E-18	1.180E-18	1.186E-18	1.161E-18	1.122E-18	9.670E-19
2.06E+08	1.110E-18	1.147E-18	1.174E-18	1.180E-18	1.164E-18	1.133E-18	9.946E-19
2.58E+08	1.106E-18	1.140E-18	1.166E-18	1.173E-18	1.163E-18	1.144E-18	1.023E-18
3.23E+08	1.097E-18	1.129E-18	1.152E-18	1.158E-18	1.151E-18	1.139E-18	1.018E-18
4.05E+08	1.095E-18	1.124E-18	1.144E-18	1.150E-18	1.147E-18	1.140E-18	1.023E-18
5.08E+08	1.094E-18	1.118E-18	1.137E-18	1.142E-18	1.139E-18	1.134E-18	1.074E-18
6.37E+08	1.090E-18	1.110E-18	1.125E-18	1.129E-18	1.124E-18	1.118E-18	1.080E-18
7.98E+08	1.099E-18	1.116E-18	1.127E-18	1.129E-18	1.124E-18	1.118E-18	1.071E-18

## A.2. Stochastic Dust Temperature Distribution

In order to calculate the temperature distribution of dust grains subject to a bath of free electrons in a hot gas, and thus the emission by such dust grains, we follow the schemes proposed by Dwek (1986) and Guhathakurta & Draine (1989) with a few extra considerations. In the Dwek’s scenario, a dust grain with an initial temperature  $T_0$ , collides with a free electron with energy  $E$  which transfers a fraction of its kinetic energy,  $\zeta(a, E)$ , to the dust particle. Depending on the size and chemical composition of the dust grain (because its heat capacity,  $C(a, T_d)$ , is a function of both), the dust particle will be heated to a peak temperature  $T_{peak}$ , which is obtained from iteration of the equation

$$\zeta(a, E)E = \int_{T_0}^{T_{peak}} C(a, T_d) dT_d. \quad (\text{A8})$$

From  $T_{peak}$ , the dust particle starts to cool down and eventually, after many collisions, it acquires thermodynamic equilibrium unless the characteristic time for electron-grain collisions is larger than the grain cooling time, in which case the grain temperature will start to fluctuate (Dwek 1986; Dwek & Arendt 1992). The grain cooling time,  $\tau_{cool}$ , between  $T_{peak}$  and some temperature  $T_d$ , is given by

$$\tau_{cool} = \int_{T_d}^{T_{peak}} \frac{C(a, T_d) dT_d}{|4\pi a^2 \sigma \langle Q_{abs} \rangle T_d^4|}, \quad (\text{A9})$$

where  $\sigma$  is the Stefan-Boltzmann constant and  $\langle Q_{abs} \rangle$  is the dust absorption efficiency,  $Q_{abs}(\lambda, a)$ , averaged by the Planck function,  $B_\lambda(T_d)$  (in terms of the wavelength,  $\lambda$ ):

$$\langle Q_{abs} \rangle = \frac{1}{\sigma T_d^4} \int_0^\infty \pi Q_{abs}(\lambda, a) B_\lambda(T_d) d\lambda. \quad (\text{A10})$$

The values of  $C(a, T_d)$  for silicate and graphite grains were taken from Dwek (1986) and from Draine & Anderson (1985), while the values of  $Q_{abs}(\lambda, a)$  were obtained from the data files provided in the DustEM code <sup>1</sup> (Compiègne et al. 2011). The characteristic time between successive electron collisions with a dust grain,  $\tau_{coll}$ , is calculated as (Bocchio et al. 2013):

---

<sup>1</sup><http://www.ias.u-psud.fr/DUSTEM>

$$\tau_{coll}^{-1} = \pi a^2 n \sqrt{\frac{3k_B T}{m_e}}, \quad (\text{A11})$$

where  $m_e$  is the mass of the electron. The fraction of time in which a dust grain can be found in the temperature interval  $T_d + dT_d$  after a collision with an electron is (Purcell 1976):

$$P(a, E, T_d, T_0) dT_d = \begin{cases} \frac{C(a, T_d)}{4\pi a^2 \sigma \langle Q_{abs} \rangle T_d^4} \frac{e^{-\tau_{cool}/\tau_{coll}}}{\tau_{coll}}, & \text{if } T_d \leq T_{peak} \\ 0, & \text{otherwise.} \end{cases} \quad (\text{A12})$$

One can obtain now the probability,  $G(a, T_d, T_0)$ , that a dust grain is to be found between  $T_d$  and  $T_d + dT_d$  if one integrates the above quantity over all the electron energies according to the Maxwell-Boltzmann distribution

$$G(a, T_d, T_0) = \pi a^2 n \tau_{coll} \int_0^\infty P(a, E, T_d, T_0) f(E) v(E) dE. \quad (\text{A13})$$

By evaluating equation A13, we obtain the temperature distribution of a population of grains with the same initial temperature  $T_0$ , size and chemical composition. In the above equation,  $f(E)$  and  $v(E)$  are the Maxwell-Boltzmann distribution of energy and the speed of the impinging electron, respectively. In order to obtain the temperature distribution of grains with a wide range of initial temperatures, we will employ the stochastic matrix method described by Guhathakurta & Draine (1989) and Marengo (2000).

Let  $\mathbf{A}_{T_d^i, T_0^j}$ , be an  $N \times N$  stochastic matrix, which describes the probability (per unit time) of a grain to make a transition between  $T_0$  and some temperature  $T_d$ . The entries of  $\mathbf{A}_{T_d^i, T_0^j}$  are obtained from evaluation of equation A13:

$$\mathbf{A}_{T_d^i, T_0^j} = \begin{pmatrix} G(a, T_d^1, T_0^1) & G(a, T_d^1, T_0^2) & \cdots & G(a, T_d^1, T_0^j) \\ G(a, T_d^2, T_0^1) & G(a, T_d^2, T_0^2) & \cdots & G(a, T_d^2, T_0^j) \\ \vdots & \vdots & \ddots & \vdots \\ G(a, T_d^i, T_0^1) & G(a, T_d^i, T_0^2) & \cdots & G(a, T_d^i, T_0^j) \end{pmatrix}. \quad (\text{A14})$$

In our case we employed a logarithmic grid for  $T_d$  and  $T_0$ , from 1 K to 1100 K and  $N = 125$ .



Let now  $G_{n=0}^i$  be an initial temperature distribution given by a column vector which comes from evaluating equation A13 with  $T_0 = T_0^{trial}$ , a trial initial temperature:

$$G_{n=0}^i = \begin{pmatrix} G(a, T_d^1, T_0^{trial}) \\ G(a, T_d^2, T_0^{trial}) \\ \vdots \\ G(a, T_d^i, T_0^{trial}) \end{pmatrix}. \quad (\text{A15})$$

We apply the stochastic matrix to the initial temperature distribution to obtain a new stochastic temperature distribution,  $G_{n=1}^i = G_{n=0}^i \mathbf{A}_{T_d^i, T_0^{trial}}$ . We continue to iteratively apply the stochastic matrix,

$$G_{n+1}^i = G_n^i \mathbf{A}_{T_d^i, T_0^j}, \quad (\text{A16})$$

until the condition  $(\mathbf{I} - \mathbf{A}_{T_d^i, T_0^j})G_{n+1} = 0$ , with  $\mathbf{I}$  the identity matrix, is fulfilled. This condition ensures that, after many discrete heating events, the temperature distribution does not change under the application of the stochastic matrix; this is the steady state temperature distribution,  $G(a, T_d)$ .

Big grains ( $\gtrsim 0.1 \mu\text{m}$ ), with large cross sections and heat capacities, are more likely to reach thermodynamic equilibrium due to very frequent collisions. In that case, their temperature distribution approaches a delta function around the equilibrium temperature,  $T_{eq}$ , which can be obtained by equating the heating and cooling rates:

$$\pi a^2 n \int_0^\infty f(E) v(E) \zeta(a, E) E \, dE = 4\pi a^2 \sigma \langle Q_{abs} \rangle T_{eq}^4. \quad (\text{A17})$$

Once the dust temperature distribution is known, the infrared flux can be calculated from equation 15 of Dwek & Arendt (1992).

## REFERENCES

- Adamo, A., Östlin, G., Zackrisson, E., et al. 2010a, MNRAS, 407, 870  
 Adamo, A., Östlin, G., Zackrisson, E., et al. 2011, MNRAS, 415, 2388

- Adamo, A., Zackrisson, E., Östlin, G., & Hayes, M. 2010b, *ApJ*, 725, 1620
- Arendt, R. G., Dwek, E., Kober, G., Rho, J., & Hwang, U. 2014, *ApJ*, 786, 55
- Barlow, M. J., Krause, O., Swinyard, B. M., et al. 2010, *A&A*, 518, L138
- Bautista, M. A., Depoy, D. L., Pradhan, A. K., et al. 1995, *AJ*, 109, 729
- Beltrametti, M., Tenorio-Tagle, G., & Yorke, H. W. 1982, *A&A*, 112, 1
- Bocchio, M., Jones, A. P., Verstraete, L., et al. 2013, *A&A*, 556, A6
- Cernuschi, F., Marsicano, F., & Codina, S. 1967, *Annales d’Astrophysique*, 30, 1039
- Chevalier, R. A., & Clegg, A. W. 1985, *Nature*, 317, 44
- Compiègne, M., Verstraete, L., Jones, A., et al. 2011, *A&A*, 525, A103
- Draine, B. T., & Anderson, N. 1985, *ApJ*, 292, 494
- Draine, B. T., & Salpeter, E. E. 1979, *ApJ*, 231, 77
- Dwek, E. 1986, *ApJ*, 302, 363
- Dwek, E. 1987, *ApJ*, 322, 812
- Dwek, E., & Arendt, R. G. 1992, *ARA&A*, 30, 11
- Dwek, E., & Arendt, R. G. 2015, *ApJ*, 810, 75
- Dwek, E., & Werner, M. W. 1981, *ApJ*, 248, 138
- Dwek, E., Arendt, R. G., Bouchet, P., et al. 2008, *ApJ*, 676, 1029
- Fisher, D. B., Bolatto, A. D., Herrera-Camus, R., et al. 2014, *Nature*, 505, 186
- Gomez, H. 2013, in *Proceedings of The Life Cycle of Dust in the Universe: Observations, Theory, and Laboratory Experiments (LCDU2013)*. 18-22 November, 2013. Taipei, Taiwan. Editors: Anja Andersen (University of Copenhagen, Denmark), Maarten Baes (Universiteit Gent, Belgium), Haley Gomez (Cardiff University, UK), Ciska Kemper (Academia Sinica, Taiwan), Darach Watson (University of Copenhagen, Denmark)., 146
- Gomez, H. L., Krause, O., Barlow, M. J., et al. 2012, *ApJ*, 760, 96
- Guhathakurta, P., & Draine, B. T. 1989, *ApJ*, 345, 230

- Guillard, P., Boulanger, F., Pineau Des Forêts, G., & Appleton, P. N. 2009, *A&A*, 502, 515
- Hirashita, H., & Nozawa, T. 2013, *Earth, Planets, and Space*, 65, 183
- Indebetouw, R., Matsuura, M., Dwek, E., et al. 2014, *ApJ Let*, 782, L2
- Izotov, Y. I., Guseva, N. G., Fricke, K. J., Krügel, E., & Henkel, C. 2014, *A&A*, 570, A97
- Laor, A., & Draine, B. T. 1993, *ApJ*, 402, 441
- Leitherer, C., Schaerer, D., Goldader, J. D., et al. 1999, *ApJS*, 123, 3
- Marengo, M. 2000, PhD thesis, International School for Advanced Studies (SISSA/ISAS), Harvard-Smithsonian Center for Astrophysics
- Mathis, J. S., Rumpl, W., & Nordsieck, K. H. 1977, *ApJ*, 217, 425
- Matsuura, M., Dwek, E., Barlow, M. J., et al. 2014, ArXiv e-prints, arXiv:1411.7381
- Matsuura, M., Dwek, E., Barlow, M. J., et al. 2015, *ApJ*, 800, 50
- Moseley, S. H., Dwek, E., Glaccum, W., Graham, J. R., & Loewenstein, R. F. 1989, *Nature*, 340, 697
- Nozawa, T., Kozasa, T., Habe, A., et al. 2007, *ApJ*, 666, 955
- Nozawa, T., Kozasa, T., Umeda, H., Maeda, K., & Nomoto, K. 2003, *ApJ*, 598, 785
- Ostriker, J., & Silk, J. 1973, *ApJ Let*, 184, L113
- Palouš, J., Wunsch, R., Martínez-González, S., et al. 2013, *ApJ*, 772, 128
- Purcell, E. M. 1976, *ApJ*, 206, 685
- Raymond, J. C., Cox, D. P., & Smith, B. W. 1976, *ApJ*, 204, 290
- Reines, A. E., Johnson, K. E., & Hunt, L. K. 2008, *AJ*, 136, 1415
- Silich, S., Bisnovatyi-Kogan, G., Tenorio-Tagle, G., & Martínez-González, S. 2011, *ApJ*, 743, 120
- Smith, R. K., Krzewina, L. G., Cox, D. P., Edgar, R. J., & Miller, III, W. W. 1996, *ApJ*, 473, 864
- Suntzeff, N. B., & Bouchet, P. 1990, *AJ*, 99, 650

- Temim, T., Sonneborn, G., Dwek, E., et al. 2012, *ApJ*, 753, 72
- Tenorio-Tagle, G., Silich, S., Martínez-González, S., et al. 2013, *ApJ*, 778, 159
- Tenorio-Tagle, G., Silich, S., Martínez-González, S., Terlevich, R., & Terlevich, E. 2015, *ApJ*, 800, 131
- Tenorio-Tagle, G., Wunsch, R., Silich, S., & Palouš, J. 2007, *ApJ*, 658, 1196
- Tielens, A. G. G. M., McKee, C. F., Seab, C. G., & Hollenbach, D. J. 1994, *ApJ*, 431, 321
- Todini, P., & Ferrara, A. 2001, *MNRAS*, 325, 726
- Tsai, J. C., & Mathews, W. G. 1995, *ApJ*, 448, 84
- Vanzi, L., Hunt, L. K., Thuan, T. X., & Izotov, Y. I. 2000, *A&A*, 363, 493
- Wooden, D. H., Rank, D. M., Bregman, J. D., et al. 1993, *ApJS*, 88, 477
- Yamada, K., & Kitayama, T. 2005, *PASJ*, 57, 611